PHYSICAL REVIEW E **77**, 036407 (2008)

Lateral movement of a laser-accelerated proton source on the target's rear surface

Tatsufumi Nakamura,[1,*] Kunioki Mima,[1] Sargis Ter-Avetisyan,[2] Matthias Schnürer,[2] Thomas Sokollik,[2] Peter V. Nickles,[2]
and Wolfgang Sandner[2]
[1]*Institute of Laser Engineering, Osaka University, 2-6 Yamadaoka, Suita, Osaka 565-0871, Japan*
[2]*Max-Born-Institute, Max-Born-Strasse 2a, D-12489 Berlin, Germany*

(Received 26 December 2007; published 18 March 2008)

The spatial dependence of proton acceleration at the rear surface of a target that is irradiated by high-contrast and ultraintense laser pulses is investigated. Lateral movement of the proton acceleration position at the rear surface is observed; this is tested by a two-pinhole measurement which results in the observation of protons with a narrow energy band. This drifting is only observed when relativistic-intensity laser pulses irradiate targets with a small preplasma at oblique incidence, as is confirmed by two-dimensional particle-in-cell simulations. This scenario of proton acceleration by the fast-moving sheath field leads to energy selection of the accelerated protons as a function of observing position.

DOI: 10.1103/PhysRevE.77.036407 PACS number(s): 52.38.Kd, 52.40.Kh

Interactions of intense laser pulses with solid targets have been investigated persistently since the advent of the chirped pulse amplification technique which enables use of ultrashort and relativistic-intensity laser pulses. Those generate high-energy-density plasmas, which have opened new research fields such as the fast-ignition scheme in inertial fusion [1], compact acceleration for high-energy charged particles and x rays [2,3], and many others.

Recently, interactions of relativistic-intensity laser pulses with targets having a sharp density edge have been realized due to the improvements of techniques to reduce the prepulse level. Interactions of the main pulse with targets with and without preplasmas are significantly different from the perspective of the dominant electron acceleration processes and the energy coupling to plasmas. These differences become pronounced in the case of oblique irradiation. In oblique irradiation, the resonance absorption plays the dominant role in energy absorption when the scale length of the preplasma is larger than the laser wavelength, which results in the generation of high-energy electrons propagating in the target-normal direction. When the preplasma is smaller, high-energy electrons are generated in the laser propagation direction also by ponderomotive acceleration with relatively small angular spread [4]. As a consequence, protons are emitted from two separate points which are attributed to the electric fields induced by the electrons accelerated in the laser propagation and target-normal directions [5]. Protons are accelerated from two separate positions by the well-known "target-normal sheath acceleration" [6,7], as long as the target is thick enough for them to be spatially distinguished. Another important phenomenon in the small-preplasma case is surface energy transport by high-energy electrons [8–10]. As the target front becomes steeper, the absorbed laser energy tends to be transported along the surface by high-energy electrons, which are confined by the surface magnetic and electric fields. The target thickness is also a key parameter characterizing the laser-matter interaction. When the target thickness is smaller than the laser pulse length, high-energy electrons generated at the target front surface are circulating inside the target and the electron density inside the target increases [11]. This leads to a higher sheath field at the target surface, which increases the sheath-accelerated proton energy [12–14]. And when the target thickness is further reduced such that it becomes comparable to the laser skin depth, the target becomes transparent, which results in ion acceleration by the greatly enhanced sheath field or directly by the laser field afterward [15,16]

In this paper, we incorporate particle diagnostics which provide a microscopic measurement of the proton acceleration with particle-in-cell (PIC) simulations and clarify the proton acceleration process that is uniquely observed for small prepulses, oblique irradiation, and in thin targets. In this case, we found that the laser-accelerated proton source drifts on the rear surface of the target in the direction of projection of the laser wave vector onto the surface. The drift of the proton source is explained by the lateral movement of the sheath field. This moving proton source leads to the observation of a limited range of proton energies at any given point along the target surface.

The proton source was investigated with an experimental setup and geometry similar to those of Ref. [17], which provides high spatial resolution. The 40 fs pulse from a Ti:sapphire laser with energy of up to 700 mJ was focused with an $f/2.5$ off-axis parabolic mirror to intensities of about 2×10^{19} W/cm^2. The intensity of the amplified spontaneous emission (ASE) pedestal of the laser pulse in several picoseconds before the pulse peak is reduced to about 10^{-8}. The temporal contrast of the laser pulse was measured with a scanning third-order cross correlator with a dynamic range of 10^{10}, having a resolution of 150 fs and a scanning range of ±200 ps. The pulse shape several nanoseconds before the main pulse was controlled by a fast photodiode with temporal evolution of about 300 ps. The ion emission spectrum was measured with an absolutely calibrated Thomson parabola spectrometer setup [18] in magnifying imaging mode [17]. In the Thomson spectrometer setup [see Fig. 1(d)] particles are dispersed in the z direction perpendicular to the magnetic field according to their energy and charge; how-

---

[*] Present address: Kansai Photon Science Institute, Japan Atomic Energy Agency, 8-1 Umemidai, Kyoto 619-0215, Japan. nakamura.tatsufumi@jaea.go.jp

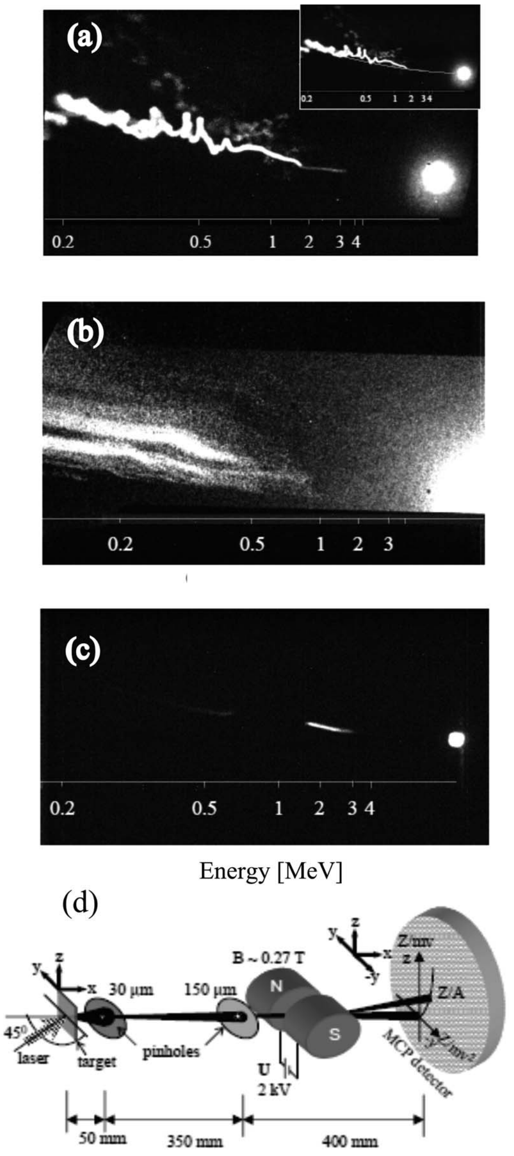

FIG. 1. (a) Charge-coupled device (CCD) picture of the proton spectrum at 45° laser incidence on a target measured in the direction of the target normal with a magnification imaging ratio of 1:15. The ideal parabola trace is the solid line in the figure inset. (b) CCD picture of the proton spectrum from a Mylar target. (c) CCD picture of the proton spectrum from a target measured in the direction of the target normal when the proton beam passes through two pinholes. The two-pinhole measurement makes it possible to detect the protons emitted only from a 16–18 μm area of the source. (d) Schematic figure of the geometry of the two-pinhole measurement.

ever, in the y direction along the magnetic field lines, the original trajectories of the particles are traceable, which allows us to use this dimension to analyze the ion source distribution. This solution is similar to a transmission grating spectrometer where the direction perpendicular to dispersion is used for the characterization of the spatial distribution of an emission source in the full spectral range. The electric field of the spectrometer (along the y direction) shifts the particles only in the y direction, in dependence on their energy, which is determined by the deflection in the magnetic field. The polarization vector of the laser is in the x-y plane as also is the laser propagation vector. The laser beam is incident at 45° to the target normal, which is in the x direction as also is the main ion propagation direction. In the spectrometer a magnetic field of about 0.27 T and electric fields of 2 kV/cm were applied. The ions are detected by a multichannel-plate detector coupled to the phosphor screen.

The spectrum is imaged through a 30 μm pinhole, located at a distance of 5 cm from the source, on a detector screen 75 cm behind the pinhole, at 45° laser incidence on a 13 μm aluminum target; see Fig. 1. The striking features of this figure are that the whole low-energy part of the spectrum is shifted from the ideal parabolic trace calculated according to our geometry, whereas the high-energy part obeys the calculated parabolic trace [solid line in Fig. 1(a) inset] assuming that the ions are emitted from a fixed ion source, and finally that the trace of the low-energy part shows strong oscillations.

The imaging factors of the setup include the geometry and the emitted proton beam characteristics, such as partial beam divergence. In Fig. 1(a) it is found that the trace spread decreases with increasing proton energy. The trace spread and the partial beam divergence calculated for the present geometry (distance from the source to the detector) decrease from 0.13 to 0.11 mrad when the proton energy increases from 0.2 to 3 MeV. Therefore, in the present geometry, the image covers only the diameter of an $\simeq 18$ μm area on the target with a magnification factor of about 15. The observed phenomena are attributed to the continuous movement of the proton emission source up to about 20 μm. When electron beam filamentation occurs during electron propagation inside the target, as is the case for insulators [19], several proton emission points and corresponding multiple parabolic traces would be measured. With the same geometry of the experimental setup, the proton spectra from 13 and 20 μm Mylar targets taken at a relatively low laser pulse contrast ($\sim 10^{-7}$) indicate many separate proton emission points on the target. In Fig. 1(b) is given, for example, a proton spectrum from a 20 μm Mylar target. Here the energy scale is calculated according to the geometry where the source point is in the middle of the right blob in Fig. 1(b). The continuous proton spectrum in Fig. 1(a) indicates that one proton source point is continuously moving on the surface. In order to give additional proof of this, a second pinhole with a diameter of 150 μm was installed at 35 cm behind the first pinhole [see Fig. 1(d)], in order to detect only the protons emitted from an area of 20 μm diameter with straight trajectories along this axis. Particles that are emitted from the other parts of the source and even have passed the first pinhole will be blocked by the second one. A continuous decrease of the size of the second pinhole led to truncation of the spectrum and finally only the high-energy part of the spectrum remains, which lies on the expected ideal parabolic trace as shown in Fig. 1(c), indicating that they are accelerated from the indicated point source. This is ultimate proof that the observed phenomena can be attributed to the source movement. Here the interesting point is that the source position from which the high-energy protons are emitted does not emit the low-energy ones. It has to be mentioned that these phenomena are observed at 45° laser irradiation and not observed in the normal-irradiation case. Continuous movement of the source could be a problem for applications, since a point source and narrow energy spectrum of protons are required. On the other hand, by selecting the emission point with the use of two pinholes one could have a bunch of protons in a certain narrow energy interval as shown in Fig. 1(c).

Two-dimensional PIC simulations were carried out to see the temporal evolution of the sheath field on the rear surface, which is related to the proton source movement, and to clarify the conditions in which the proton source moves along the surface. The simulation conditions are as follows. The targets are 13 μm in thickness and 70 μm in width with density of $40n_c$, where n_c denotes the critical density for the laser wavelength of 0.8 μm, and consist of electrons and Al^{3+} ions. The proton source is a contaminant layer, which is modeled as a buried proton layer at the rear surface with thickness of 0.1 μm and density of $1n_c$, i.e., the 0.1 μm layer from the rear surface is composed of $39n_c$ of Al^{3+} and $1n_c$ of protons, with $40n_c$ electrons. The electrons initial temperature is set at 1 keV, and the ions are initially cold. The system size is 50 μm in the x direction and 70 μm in the y direction, and the cell number is 2245×3369. 12 particles are used in one mesh for each species and the total number of particles is about 8×10^7. The density profile of the preplasma is assumed to be exponential with two scale lengths. For the overdense region where the density is higher than $3n_c$ the scale length is 0.1 μm. For the lower-density region, lower than $3n_c$, the scale length is 0.5 or 3.5 μm. A p-polarized laser pulse whose spot diameter is 10 μm irradiates the target from the left boundary with the incident angle of 45°. The laser pulse ramps up in five laser cycles and sustains its peak intensity of 2.0×10^{19} W/cm^2 for the pulse duration of 40 fs. The laser axis irradiates the target surface at $y \simeq 17$ μm. On the boundaries, particles are reflected back to the system by reducing their energy to the thermal one, and the electromagnetic fields are damped at the boundaries.

The temporal evolution of the longitudinal electric field E_x and electron energy density distribution for the small-preplasma case (0.5 μm length scale in the lower-density region) are shown in Fig. 2. The region where electron energy density is high moves upward; this direction of movement is explained as follows. The high-energy electrons are accelerated in the laser propagation direction by ponderomotive acceleration for the small-preplasma case. When they exit from the rear surface, very energetic electrons escape from the target, but a large number of the electrons are dragged back and reinjected into the target toward the front side. As a result, electrons move upward, being trapped along the target. Thus the direction of movement of the high-energy-density region is the projection direction of the laser wave vector onto the surface. Since the longitudinal electric field is induced by the high-energy electrons, the sheath field also moves in the same direction, as is seen in Fig. 2, which results in the movement of the proton acceleration point. There are two components of the sheath fields showing different time evolutions. The sheath field induced by electrons accelerated in the target-normal direction by vacuum heating is symmetric around the target-normal position and expands radially, quickly reducing its magnitude. Another component is generated by electrons accelerated by ponderomotive acceleration, with greater magnitude than the previous one, since the ponderomotively accelerated electrons have much higher energy than target-normal electrons as is shown in Fig. 4(a) below and also in Ref. [20]. At the early time of irradiation, a rather symmetrically expanded sheath field is induced. Shortly thereafter, a stronger sheath field localized at the ponderomotive position ($y \sim 29$ μm) is induced, while the symmetric field is weakened by diffusion [Fig. 2(d)]. The sheath field is strongest at the ponderomotive position and

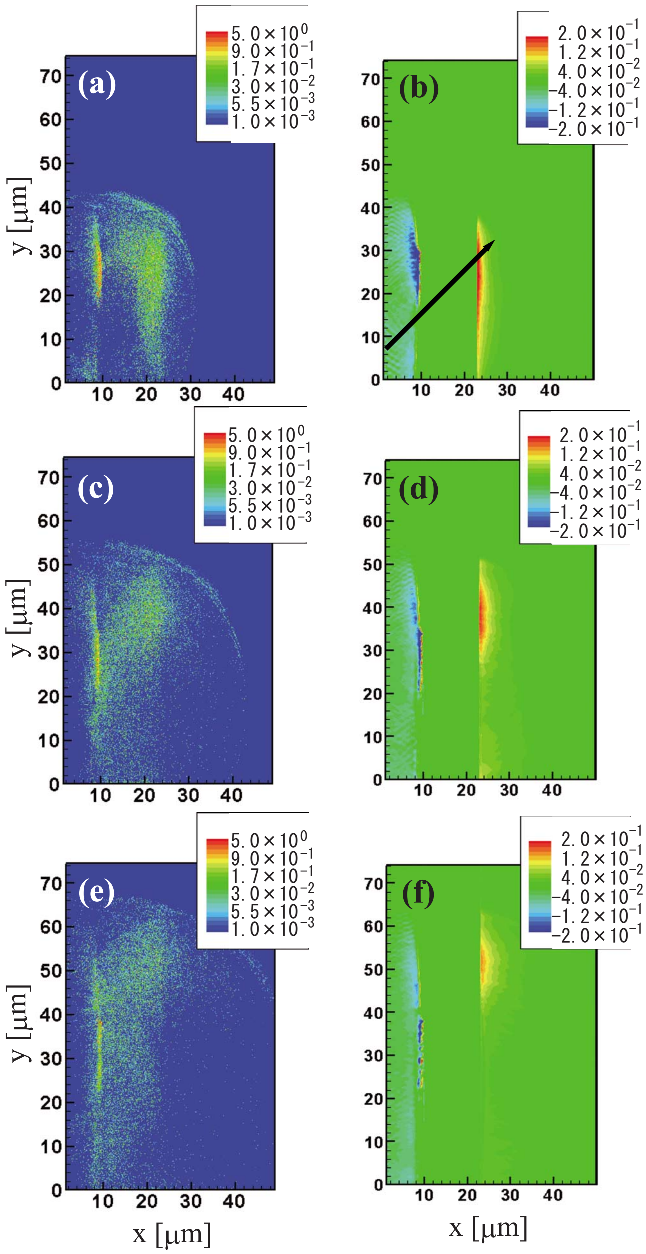

FIG. 2. (Color online) Temporal evolution of the electron energy density and the longitudinal electric field. The electron energy density is normalized by $n_c mc^2$, and observed at (a) 140, (c) 180, and (e) 220 fs. The electric field is normalized by the laser electric field, and observed at (b) 140, (d) 180, and (f) 220 fs. The target width is 13 μm and is located at $10 < x < 23$ μm. The black line in (b) indicates the laser axis.

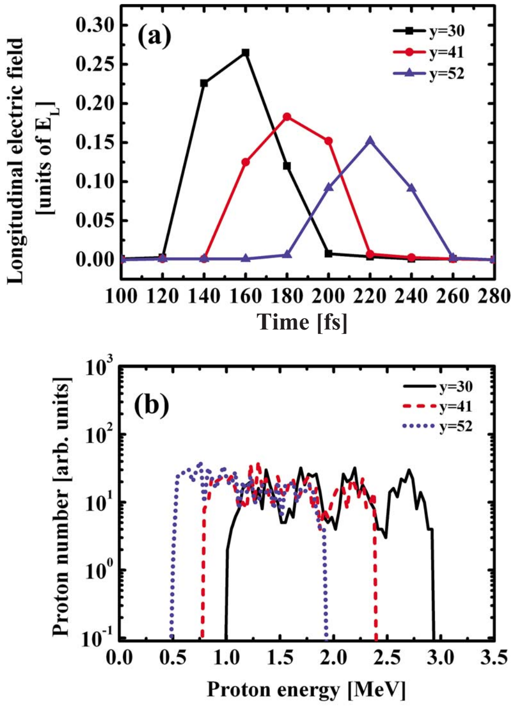

FIG. 3. (Color online) (a) Temporal evolutions of maxima of sheath field intensity at different positions $y=30$, 41, and 52 μm. (b) Proton energy spectra observed at three positions chosen the same as in (a). The observation timings are delayed for the upper position such that $t=400$, 440, and 480 fs at $y=30$, 41, and 52 μm, respectively, since there is a time delay before the sheath field reaches and starts to accelerate protons.

has a size comparable to the laser spot size. The temporal evolutions of the maximum of the sheath field intensities at different positions are compared in Fig. 3(a), where the ponderomotive position ($y\sim 29$ μm), and 11 and 22 μm upward to the position (i.e., $y=41$ and 52 μm) are chosen. As is seen from the figure, the intensity of the sheath field decreases as it propagates upward with velocity roughly close to the speed of light. The energy spectra of accelerated protons observed at those positions with 2 μm width are shown in Fig. 3(b). In the figure, the time delay of the proton acceleration due to the sheath movement is taken into account. It is seen that protons with the highest energies ($2.3\leq E \leq 3.0$ MeV) are accelerated at the ponderomotive position by the strong sheath field, and protons accelerated in the upper position by the weakened field have lower energies.

Since the lateral movement of the region of high electron energy density is due to the lateral movement of ponderomotively accelerated electrons, the scale length of the preplasma is crucial for the drift since the dominant acceleration process depends on the scale length. The angular distributions of electron momentum inside the targets are compared for two different scale lengths, i.e., 0.5 and 3.5 μm, shown in Figs. 4(a) and 4(b). In the small-preplasma case, the high-energy electrons are well collimated and accelerated along the laser propagation direction by the ponderomotive acceleration. On the other hand, in the large-preplasma case, the electrons are dominantly accelerated toward the target-normal direction by the resonance absorption. In this case, the electrons propagating away from the rear surface return to the target in every direction like a fountain, which results in the symmetric expansion of the sheath field. As a result, in the large-preplasma case, directional lateral drift of the sheath field and proton source movement are not observed.

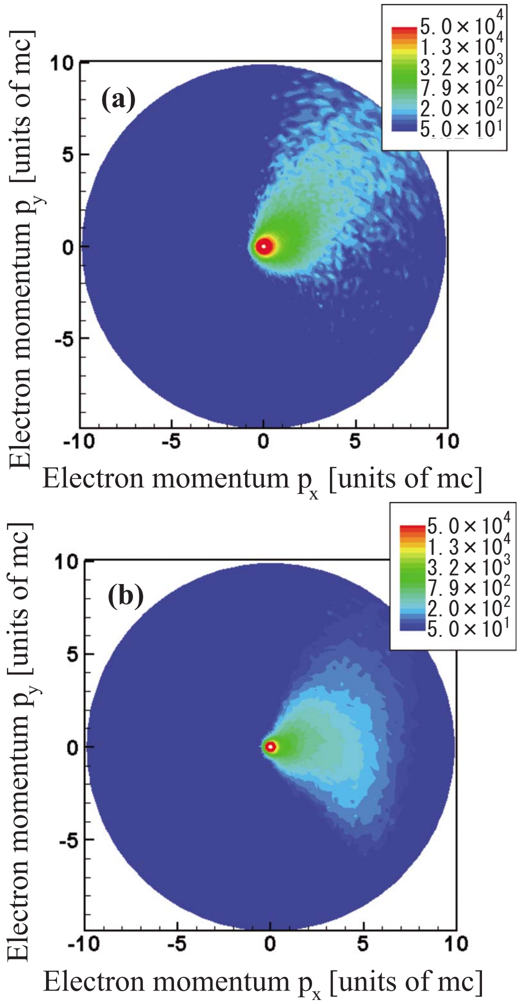

FIG. 4. (Color online) Angular distribution of laser-accelerated electrons for scale length of preplasma (a) 0.5 and (b) 3.5 μm.

The target thickness is also an important parameter. The lateral movement of the sheath field becomes less effective as the target thickness increases, since the electron energy density at the target surface decreases due to the expansion of the high-energy electrons into the target. Therefore, the target thickness is chosen to be comparable to or less than the laser pulse length for effective lateral drift of the sheath field. Also, the laser intensity is required to be relativistic so that the ponderomotive acceleration becomes dominant, generating a directional electron beam toward the laser propagation direction.

A number of experiments on laser-proton acceleration have been carried out with similar parameters in terms of the laser intensity, irradiation angle, pulse duration, and target material and thickness [21–23]. But lateral drift of the sheath field has not been observed. The critical difference is the level of ASE. In the above cited experiments, the ASE level is mentioned as $\sim 4\times10^{12}$ W/cm^2, and in our experiments the ASE is reduced to $\sim 1\times 10^{11}$ W/cm^2 by use of a specifically delayed pump mode with a comparable duration. Thus the amount of energy of the ASE is lowered by roughly 1/40 in our experiments, which leads to the estimated scale length being lowered by 1/6. In the numerical simulations in Fuch *et al.*'s paper [21], which show good agreement with the experimental results, the scale length is set at 3 μm, which is consistent with the scale length of 0.5 μm in our experimental conditions. Finally, we want to mention the oscillation in the parabolic trace for the low-energy part. This might be attributable to the complex electron transport coupled to self-induced electric and magnetic fields on the rear surface. In the above simulations, a magnetic field of $\sim$30 MG and electric field of $\sim$1 TV/m are observed, induced by the lateral transport of high-energy electrons with an estimated current of roughly tens of kiloamperes. This surface current would be disturbed by a Weibel-like instability [24], whose wave vector lies dominantly in the z direction, which is not taken into account in a two-dimensional (2D) simulation. Its understanding and consideration of 3D effects are left for future work.

In conclusion, we have shown a scenario of proton acceleration by a fast-moving rear surface sheath field. This is observed as a directional shift of a single parabolic line, indicating that the proton emission point is drifting along the surface, which is proved by a two-pinhole measurement. This drift is confirmed by 2D PIC simulations which clarify the mechanism and conditions for the drift. The drift is only observed when intense laser pulses obliquely irradiate targets with small preplasmas. In this case, ponderomotively accelerated electrons propagate along the target and induce a comoving sheath field. This drift of the acceleration position leads to a well-characterized proton beam with protons selected by their energies as a function of the observation point, which might shed light on the control of laser-accelerated proton energy.

This work is partly supported by a Grant-in-Aid from the Science Research Foundation No. 15GS0214 by the Ministry of Education, Culture, Sports, Science, and Technology (MEXT) of Japan, a Grant-in-Aid for Young Scientists (B) No. 18740351 by MEXT of Japan, and the DGF-Sonderforschungsbereich Transregio Grants No. TR18 and No. GK 1203, and with the help of the Computation Group at ILE and the ITBL Project at JAEA.

[1] M. Tabak *et al.*, Phys. Plasmas **1**, 1626 (1994).

[2] T. Katsouleas, Nature (London) **432**, 510 (2004), and references therein.

[3] K. Ta Phuoc, A. Rousse, M. Pittman, J. P. Rousseau, V. Malka, S. Fritzler, D. Umstadter, and D. Hulin, Phys. Rev. Lett. **91**, 195001 (2003).

[4] W. L. Kruer and K. Estabrook, Phys. Fluids **28**, 430 (1985).

[5] S. Ter-Avetisyan and P. Nickles, JETP Lett. **83**, 206 (2006).

[6] S. P. Hatchett *et al.*, Phys. Plasmas **7**, 2076 (2000).

[7] S. Wilks *et al.*, Phys. Plasmas **8**, 542 (2001).

[8] T. Nakamura, S. Kato, H. Nagatomo, and K. Mima, Phys. Rev. Lett. **93**, 265002 (2004).

[9] R.J. Mason, E.S. Dodd, and B.J. Albright, Phys. Rev. E **72**, 015401(R) (2005).

[10] B. T. Bowes *et al.*, Opt. Lett. **31**, 116 (2006).

[11] Y. Sentoku *et al.*, Phys. Plasmas **10**, 2009 (2003).

[12] M. Kaluza, J. Schreiber, M. I. K. Santala, G. D. Tsakiris, K. Eidmann, J. Meyer-ter-Vehn, and K. J. Witte, Phys. Rev. Lett. **93**, 045003 (2004).

[13] D. Neely *et al.*, Appl. Phys. Lett. **89**, 021502 (2006).

[14] J. Fuchs *et al.*, J. Phys. IV **133**, 1151 (2006).

[15] Q. L. Dong, Z. M. Sheng, M. Y. Yu, and J. Zhang, Phys. Rev. E **68**, 026408 (2003).

[16] L. Yin *et al.*, Phys. Plasmas **14**, 056706 (2007).

[17] J. Schreiber *et al.*, Phys. Plasmas **13**, 033111 (2006).

[18] S. Ter-Avetisyan, M. Schnrer, and P. V. Nickles, J. Phys. D **38**, 863 (2005).

[19] J. Fuchs *et al.*, Phys. Rev. Lett. **91**, 255002 (2003); M. Manclossi, J. J. Santos, D. Batani, J. Faure, A. Debayle, V. T. Tikhonchuk, and V. Malka, *ibid.* **96**, 125002 (2006).

[20] Z. M. Sheng, Y. Sentoku, K. Mima, J. Zhang, W. Yu, and J. Meyer-ter-Vehn, Phys. Rev. Lett. **85**, 5340 (2000).

[21] J. Fuchs *et al.*, Nature (London) **2**, 45 (2006).

[22] T. E. Cowan *et al.*, Phys. Rev. Lett. **92**, 204801 (2004).

[23] M. Hegelich *et al.*, Phys. Rev. Lett. **89**, 085002 (2002).

[24] E. S. Weibel, Phys. Rev. Lett. **2**, 83 (1959).